

Investigation of the roles of lignin in biomass-based hydrogel for efficient desalination

Qizhao Shao^{*}, Lan Sun^{*}, Xinzhou Wu, Dafeng Zheng (✉)

School of Chemistry and Chemical Engineering, Guangdong Engineering Research Center for Green Fine Chemicals, South China University of Technology, Guangzhou 510640, China

© Higher Education Press 2023

Abstract The shortage of freshwater has become a global challenge, and solar-driven interfacial evaporation for desalination is a promising way to alleviate the crisis. To develop highly efficient and environmentally friendly photothermal evaporator, the hydroxyethyl cellulose (HEC)/alkaline lignin (AL)/graphene oxide (GO) hydrogels (CLGs) with remarkable evaporative performance were successfully fabricated by a facile sol–gel method using biomass residues. The influence of AL content on the physicochemical properties of the evaporator was investigated. The increasing content of AL improves the mechanical properties, saturated water content and crosslink density of the hydrogels. The designed materials exhibit outstanding thermal insulation capacity (the thermal conductivity of less than $0.05 \text{ W}\cdot\text{m}^{-1}\cdot\text{K}^{-1}$) and high light absorption capacity of more than 97%. The solar evaporation efficiency and water evaporation rate of the HEC/64 wt % of AL/GO hydrogels (CLG4) achieve 92.1% and $2.55 \text{ kg}\cdot\text{m}^{-2}\cdot\text{h}^{-1}$ under 1 sun, respectively. The salt resistance test results reveal that the evaporation rate of the CLG4 can still reach $2.44 \text{ kg}\cdot\text{m}^{-2}\cdot\text{h}^{-1}$ in 3.5 wt % NaCl solution. The solar evaporation rate of the CLG4 can maintain in the range of $2.45\text{--}2.59 \text{ kg}\cdot\text{m}^{-2}\cdot\text{h}^{-1}$ in five cycles. This low-cost lignin-based photothermal evaporator offers a sustainable strategy for desalination.

Keywords lignin, photothermal, cellulose, desalination, hydrogel

1 Introduction

For the past centuries, freshwater scarcity has been one of

the major challenges of humanity and is compounded by increasing drought and worldwide desertification [1,2]. Water is an essential resource for life, economic development and social progress. Although water resources cover 75% of the earth, less than 3% of freshwater can satisfy the life activities of plants, animals and humans [3,4]. The human demand for freshwater has been constantly increasing with the development of modern society, and various methods such as time-limited water supply, recycling of wastewater and inter-basin water transfer have been used to alleviate freshwater shortage, but the number of people suffering from the problem of freshwater scarcity is still increasing [5,6]. According to the report of the World Health Organization, half of the population of the world will face a lack of freshwater by 2025 [7]. Presently, desalination is considered as one of the promising ways to alleviate the shortage of freshwater for households and agriculture [8,9]. Up to now, many methods, such as multi-stage flash distillation [10], reverse osmosis [11] and low-temperature multi-effect distillation [12], have been widely reported. However, these traditional desalination technologies are accompanied by a lot of obstacles such as lack of operational flexibility, expensive price and extensive energy losses, making them challenging to implement globally [13,14]. Therefore, developing efficient, low-energy, economic and pollution-free desalination processes has attracted tremendous attention from researchers. Over the past few decades, solar-driven interfacial evaporation technology has been one of the most intensive areas of academic research and industrialization efforts, which is one of the most potential and sustainable ways to mitigate the shortage of clean water resources [15,16].

The photothermal effect is caused by light excitation, resulting in the production of part or all of the heat energy. Both the absorption of sunlight and the efficiency with which it is converted into thermal energy contribute to the total photothermal performance of high-efficiency solar collector materials [17,18]. Inspired by solar-driven

Received December 20, 2022; accepted February 3, 2023; online June 2, 2023

E-mail: zhengdf@scut.edu.cn

* These authors contributed equally to this work.

desalination, researchers have improved the solar evaporation systems, designed efficient materials, and developed novel solar desalination technologies [19,20]. According to the different interaction mechanisms between electromagnetic radiation and matter, the photothermal materials are classified into three categories: plasmonic resonance materials, semiconductor materials and carbon-based materials, with the reaction mechanisms of plasmonic resonance heating of metals, non-radiative relaxation of semiconductors and thermal vibration of molecules, respectively [21,22]. Liu et al. [23] prepared a bioinspired and reusable Au nanoparticle film. The synthesized photothermal film possessed only 85% of light absorption in the wavelength range of 400–800 nm, and just 77.8% solar evaporation efficiency of the film achieved when the light intensity was $4 \text{ kW}\cdot\text{m}^{-2}$. Joo et al. [24] synthesized metal–silicon nanowires (Si-NWs) with hybrid structures to overcome the low light absorption limit of Si. It was reported that $1.12 \text{ kg}\cdot\text{m}^{-2}\cdot\text{h}^{-1}$ of the evaporation rate and 72.8% of evaporation efficiency were obtained at a light intensity of $1 \text{ kW}\cdot\text{m}^{-2}$ due to the unique photothermal properties of the Si-NWs. Huang et al. [25] reported a biphasic Cu_xS nanorod multifunctional solar evaporator with a three-dimensional hierarchical structure. The solar evaporation efficiency and water evaporation rate of the Cu_xS evaporator were 95.4% and $1.96 \text{ kg}\cdot\text{m}^{-2}\cdot\text{h}^{-1}$, respectively, owing to the efficient light capture performance and synergistic photothermal conversion properties of the Cu_xS nanorod. Zhang et al. [26] fabricated bamboo blocks loaded with polypyrrole (PPy) for a solar interfacial evaporator, which exhibited high light absorption performance in the wavelength range of 500–2400 nm. The water evaporation rate of the synthesized material reached $1.125 \text{ kg}\cdot\text{m}^{-2}\cdot\text{h}^{-1}$ under 1 sun irradiation. Based on the above literature, expensive plasma metals and environmentally harmful semiconductors were used in photothermal evaporators, which may be contrary to the purpose of preparing environmentally friendly and low-cost photothermal conversion materials.

As the second largest biomass resource, lignin is widely available and rich in functional groups (hydroxyl, carbonyl and methoxy), which facilitate further chemical modification and can be manufactured into a variety of functional materials, including water-reducing agents [27], oil–water separation materials [28], adsorbents [29], fluorescent agent [30] and antibacterial materials [31]. However, there are still gaps, such as complex preparation processes and low lignin addition, in the application and expectations of lignin in solar-driven evaporation systems as reported by current researchers. Jiang et al. [32] designed a bilayer lignin/PPy hydrogel evaporator with a three-dimensional meso/microporous structure, exhibiting an evaporation rate of $2.25 \text{ kg}\cdot\text{m}^{-2}\cdot\text{h}^{-1}$ and solar evaporation efficiency of 91.87% under 1 sun irradiation. Besides, no salt crystallization and clogging

were observed on the surface of the lignin/PPy hydrogel after 24 h of continuous operation. Nevertheless, much time was consumed by the complicated preparation method and the lignin content is only 16 wt %. Zhao et al. [33] prepared an organic film containing lignin nanoparticles (L-NPs/poly(vinyl alcohol) (PVA)) inspired by the conjugated structure in melanin. The water evaporation rate of L-NPs/PVA is only $1.62 \text{ kg}\cdot\text{m}^{-2}\cdot\text{h}^{-1}$ and the photothermal conversion efficiency can at most reach 88%. The slower evaporation rate and poor conversion efficiency limit its potential application in practical scenarios. Although photothermal conversion capability has been demonstrated in lignin, the poor light absorption ability hinders the potential application of lignin, and the lower water evaporation rate of lignin-based photothermal materials reported in the literature need further enhancement. Taking into account the fantastic features of graphene oxide (GO), such as high specific surface area, fast electron mobility, robust mechanical qualities, chemical durability and the typical π – π^* structure in crystal lattice, makes it a probable application in improving the undesirable photothermal performance of lignin.

In this work, the hydroxyethyl cellulose (HEC)/alkaline lignin (AL)/graphene oxide (GO) hydrogels (CLGs) with superior evaporation properties were successfully fabricated by a facile sol–gel method using AL and HEC as raw materials, GO as a photothermal agent, and epichlorohydrin (ECH) as a crosslinking agent. The porous structure in the hydrogel can diminish the thermal conductivity of the material. The water-carrying capacity of the prepared photothermal materials can be regulated by hydrophobic functional groups of AL. Also, the photothermal performance of the evaporator is enhanced by the synergistic effect of AL and GO. The effects of lignin content on the mechanical properties, water contact angle, pore size, apparent density and the thermal conductivity of the CLGs were investigated. The evaporation performance of the CLGs was measured under different sunlight intensities, and the salt resistance of the CLG4 (HEC/64 wt % of AL/GO hydrogels) was performed in different concentrations of NaCl solutions. The optimal evaporation rate ($2.55 \text{ kg}\cdot\text{m}^{-2}\cdot\text{h}^{-1}$) and solar evaporation efficiency (92.1%) were obtained when the mass fraction of lignin was 64 wt %. This low-cost lignin-based photothermal evaporator provides a new pathway for synthesizing novel and efficient photothermal materials and a sustainable strategy for desalination.

2 Experimental

2.1 Materials

AL (weight average molecule weight 4500 Da, polydispersity degree 2.20) was purchased from Xiangjiang Paper Co., Ltd. (Hunan, China). HEC (high viscosity,

5000–6400 mPa·s, 25 °C), GO (99%) and ECH (C_3H_5ClO , 98%) were received from Macklin Biochemical Co., Ltd. (Shanghai, China). C_2H_5OH (99.7%), NaOH (95%) were purchased from Guangzhou Chemical Reagent Factory (Guangzhou, China). All reagents were used directly as received.

2.2 Preparation of CLGs

Briefly, the AL-HEC hydrogel was synthesized by a simple sol–gel method using GO as a photothermal agent and EHC as the crosslinking agent. HEC and AL are raw materials. In a typical process, an amount of AL was air-dried at 333 K for 24 h. Then 0.2 g of HEC and 0.1 g of AL were added to 10 mL of NaOH solution (10 wt %) containing 0.02 g of GO and stirred for 6 h. Subsequently, 0.6 mL of ECH was added under continuous stirring. Then the mixture was transferred to the mold and allowed to set for 24 h to obtain hydrogel. The prepared hydrogel was immersed in C_2H_5OH and deionized water

for 12 h each to remove impurities and freeze-dried.

The reaction mechanism of the CLGs is as follows: first, the HEC is stripped of its chlorine atom to form an ether bond with a hydroxyl group, and the ring-opening epoxy group then forms an ether bond with another hydroxyl group to form a dense crosslinked network, in which the hydroxyl group comes from AL, HEC and GO, respectively. The preparation process and reaction mechanism of the CLG1 are illustrated in Fig. 1. Based on previous literature, the structure of the internal crosslinking network in the hydrogel is related to the amount of monomer [34,35]. Therefore, CLGs with different contents of AL were prepared to investigate their effects on the internal crosslinked network structure of the hydrogel. The raw material formulations and economic cost of the CLGs are shown in Table S1 (cf. Electronic Supplementary Material, ESM). The CLG2, CLG3, CLG4, and CLG5 were synthesized under the same conditions as CLG1, but the amount of the AL was 0.2, 0.3, 0.4, and 0.5 g, respectively.

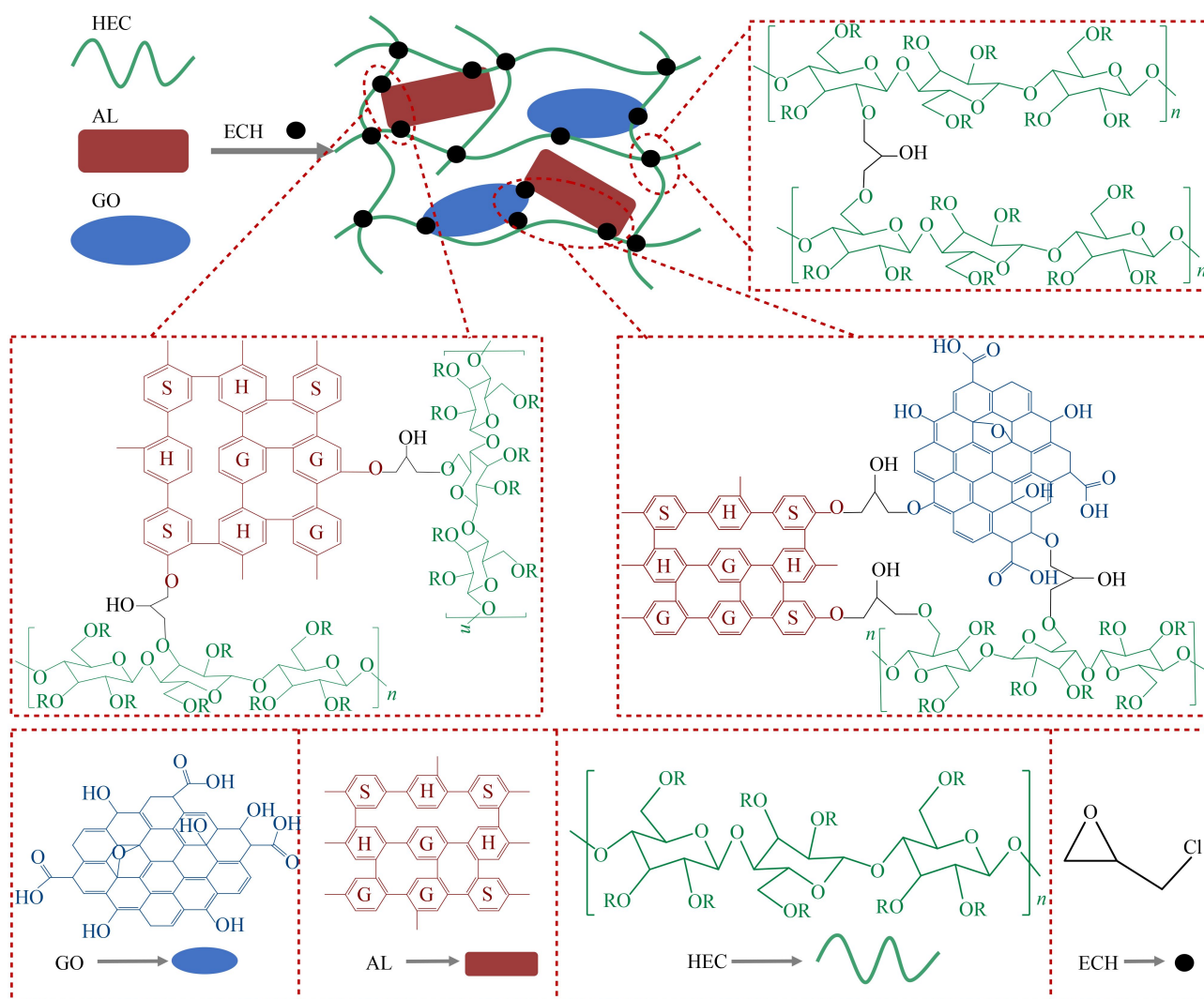


Fig. 1 The preparation process and reaction mechanism of the CLG1.

2.3 Characterization

The microstructure of the hydrogels was investigated by field-emission scanning electron microscopy (FESEM SU-8220, Hitachi, Japan) with an accelerating voltage of 5 kV, and the sample was cut into a rectangular in order to detect the internal morphology of the hydrogel. The Fourier transform infrared spectrum (FTIR, Nicolet IS50, USA) of the CLGs was characterized in the range of 4000–400 cm^{-1} . The water contact angles were measured by a contact angles meter (SDC-350, China) at room temperature. A HAAKE MARS III rheometer was used to determine the elastic modulus of the hydrogels (test temperature: 25 °C, frequency range: 0.01592–15.92 Hz). Thermal conductivity of the CLGs was tested by Hot Disk TPS 2500 thermal conductivity meter under dry state. Differential scanning calorimetry (DSC Q20, USA) was used to measure the enthalpy of evaporation of pure water and water contained in the network of hydrogels in the range of 30–200 °C.

2.4 Apparent density and swelling ratio measurements

First, the sample was cut into a rectangular shape, then the length, width and height were measured three times with a vernier caliper to calculate the apparent volume V of the sample. The mass M of the sample is measured with an electronic balance, and the apparent density of the CLGs is calculated by Eq. (1):

$$\rho = \frac{M}{V}, \quad (1)$$

where M , V and ρ represent the mass (g), volume (cm^3) and apparent density ($\text{g}\cdot\text{cm}^{-3}$) of the CLGs, respectively.

The samples were immersed in deionized water for more than 12 h to reach the dissolution equilibrium, wiped off the water on the surface of the samples and put into the electronic balance for weighing. This process was repeated three times. The swelling ratio of the sample was calculated using Eq. (2):

$$SR(\text{g}\cdot\text{g}^{-1}) = \frac{W_1 - W_0}{W_0}, \quad (2)$$

where $SR(\text{g}\cdot\text{g}^{-1})$, W_0 and W_1 denote the swelling ratio, dry weight and wet weight of the hydrogels, respectively.

2.5 Evaporation performance, solar evaporation efficiency, and equivalent enthalpy of evaporation

The samples were made into 1.5 cm \times 1.5 cm \times 1.0 cm sized squares, insulated with 1 cm thick polystyrene foam and then fixed in 100 mL beakers and subsequently placed in a simple distillation device for the solar-driven desalination experiments. Water evaporation experiments were performed in a 100 mL medium beaker. The change in the mass of water was recorded using an electronic balance. Three measurements were performed for each

sample, and the average value was taken as the exact value.

The solar evaporation efficiency is calculated by Eq. (3):

$$\eta = \frac{mh_v}{C_{\text{opt}}q_i}, \quad (3)$$

where m is the evaporation rate of water ($\text{kg}\cdot\text{m}^{-2}\cdot\text{h}^{-1}$), h_v is the evaporation enthalpy of water in the gel network ($\text{kJ}\cdot\text{g}^{-1}$). C_{opt} is the optical concentration on the surface of the CLGs, and q_i represents the radiant energy of 1 sun ($\text{kW}\cdot\text{m}^{-2}$).

Water, moist photothermal material and supersaturated potassium bicarbonate solution (humidity stabilized at about 45%) with the same surface area were simultaneously placed in a closed vessel at a temperature of 25 °C. The equivalent evaporation enthalpy is calculated from Eq. (4):

$$U_{\text{in}} = \Delta H_{\text{vap}} \times m_0 = \Delta H_{\text{equ}} \times m_g, \quad (4)$$

where U_{in} is the total equivalent energy input, ΔH_{vap} and ΔH_{equ} are the evaporation enthalpy in water and CLGs, respectively. m_0 and m_g are the mass change before and after evaporation of water and water within the hydrogels, respectively.

3 Results and discussion

3.1 Surface morphology of the CLGs

The internal structure and surface morphology of the CLGs were detected by scanning electron microscopy (SEM, Fig. 2), and significant differences are discovered in the interior and external surfaces of the CLGs. The interior pores of the CLGs display a lamellar and “honeycomb” structure, while many wrinkles and skeletons are found on the surface of the hydrogels. The explanation can be linked to a change in the morphology of cellulose in solution caused by the inner wall of the container and the surface tension of the liquid [36]. A considerable number of pore structures are observed in the internal CLGs, which can be served as water transport channels and provide capillary forces, as illustrated in Figs. 2(a), 2(c), 2(e), 2(g) and 2(i). Furthermore, the hydrogen bonding between reactants is enhanced as the lignin concentration increases, resulting in a tighter three-dimensional structure inside the aerogel as more lignin molecules are packed in the holes and CLGs pore size is reduced, which is crucial for continuous water supply and effective solar-driven water vapor production [37]. The irregular and rough surface of the CLGs (Figs. 2(b), 2(d), 2(f), 2(h) and 2(j)) provides an abundance of optical traps for the photothermal conversion process. The light is scattered several times, expanding the scattering area when sunlight irradiates the surface of the material. A bigger light

reception area traps incoming light on the surface of material and boosts the light absorption capacity of the hydrogels, facilitating the following photothermal reaction [38].

3.2 Mechanical properties of the CLGs

The internal mechanical properties of CLGs are characterized by elastic modulus (G') tests, which reflect the internal cross-link density and elastic properties of the

materials, and is commonly used to ascertain the solid-like behavior of the hydrogels [39,40]. The relationship between the G' and compression frequency of the CLGs is shown in Fig. 3. The result indicates that the G' of the CLGs rises as the AL content increases, owing to more crosslinking sites, higher crosslinking density and tighter network topology of the material, which brings about the higher mechanical strength of the hydrogels [41].

3.3 FTIR

The surface functional group of the HEC and AL, as well as CLG1–CLG5 were determined by FTIR (Fig. 4). The strong absorption peaks at 3454 cm^{-1} in the HEC molecule correspond to the stretching of $-\text{OH}$, the peaks at 2930 cm^{-1} can be ascribed to the stretching vibrations of the $\text{C}-\text{H}$, and the peaks appear at 1043 cm^{-1} are attributed to the $\text{C}-\text{O}$ stretching vibration (Fig. 4(a)). Abundant surface chemical bonds are also observed in AL. The stretching vibration of $-\text{OH}$, $\text{C}-\text{H}$ and $\text{C}=\text{O}$ can be seen in the bands at 3377 , 2930 and 1721 cm^{-1} . Two peaks at 1508 and 1458 cm^{-1} represent the vibrational absorption peaks of the aromatic skeleton in AL. The peaks at 1367 , 1258 and 1130 cm^{-1} correspond to the three fundamental structures of the lignin, which are lilac type (S), guaiac type (G) and *p*-hydroxyphenyl type (H) (Fig. S1, cf. ESM) [42]. The typical absorption peaks of both compounds (HEC and AL) are contained in CLG4. The intensity of the hydroxyl absorption peak of the CLG4 diminishes due to the involvement of the hydroxyl group acts as a crosslinking site in the reaction. Besides, the absorption peaks of aromatic and aliphatic ethers are found at 1120 and 1057 cm^{-1} , indicating a successful crosslinking process involving AL, HEC and GO. The FTIR spectra of CLG1–CLG5 are displayed in Fig. 4(b). Obviously, similar absorption peaks can be discovered on the surface of the CLGs. The peaks range from 3400 to 3500 cm^{-1} represent the stretching vibration peak of the hydroxyl group. Moreover, the intensity of the hydroxyl absorption peak dropped as lignin concentration increased, indicating a rise in crosslinking sites in the gel

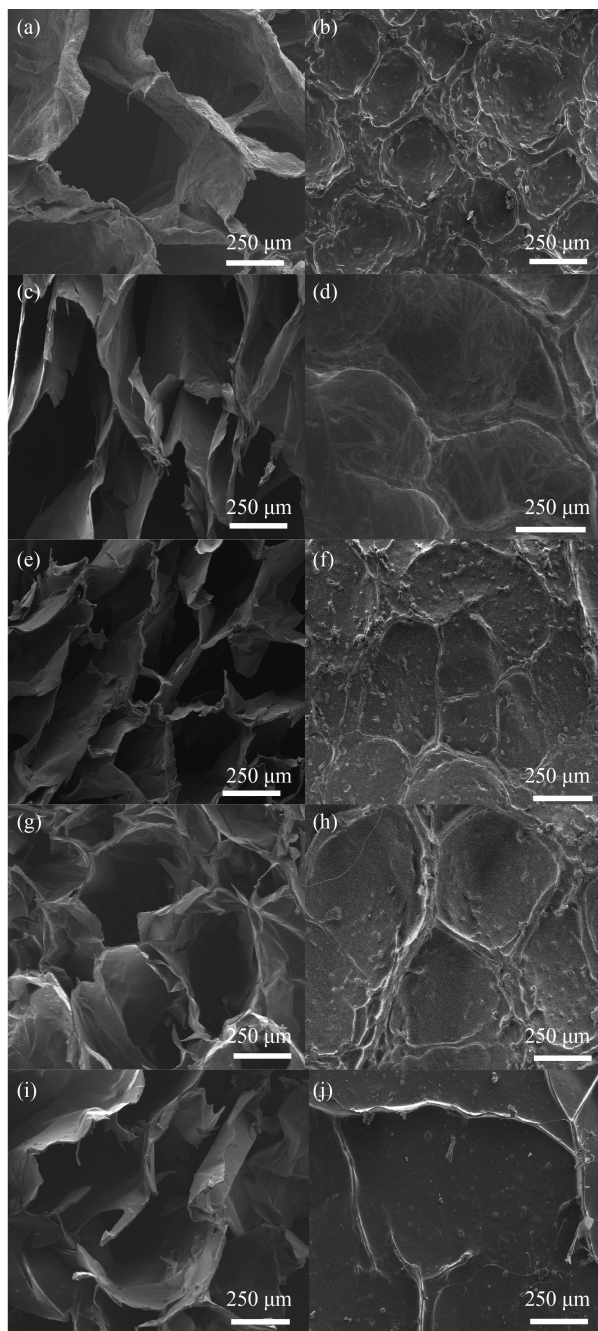


Fig. 2 SEM images of the (a, c, e, g and i) interior and (b, d, f, h and j) surface of the CLGs: (a, b) CLG1, (c, d) CLG2, (e, f) CLG3, (g, h) CLG4, (i, j) CLG5.

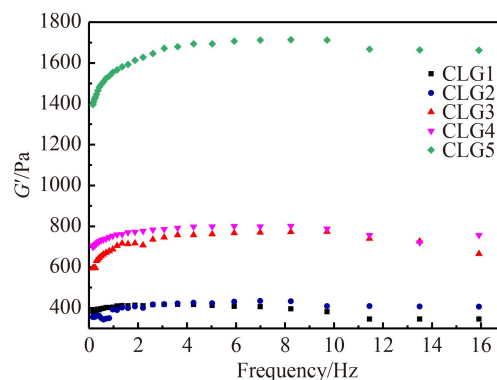


Fig. 3 Elastic moduli G' as a function of frequency measured.

network and a consequent enhancement of the cross-linking density, which is consistent with the results of the mechanical performance tests [43].

3.4 Hydrophilicity test of the CLGs

Efficient water evaporation processes require that the photothermal materials can efficiently absorb and transport water to the surface of the evaporator. Although the surface of the CLGs is rough after freeze-drying, SEM results demonstrate the existence of an extensive pore structure inside the CLGs. The water contact angles on the surface and interior of the CLGs were measured individually to assess the water transportation ability, as shown in Fig. 5. The surface contact angles of the five hydrogels are illustrated in Fig. 5(a). The order of the water contact angle for different samples is CLG5 (84°) > CLG4 (64°) > CLG3 (61°) > CLG2 (48°) > CLG1 (40°), the size of the water contact angle and lignin content were positively associated because of the hydrophobic structure (such as aromatic structure) included in lignin, but still less than the critical value of 90°. The internal wettability test of the CLGs at different time is shown in Fig. 5(b). A drop of water (2 μL) can be completely absorbed within 4 ms, indicating a superior hydrophilicity within the CLGs, which is favorable to the transport of water during the photothermal evaporation process.

3.5 Apparent density and swelling ratio of the CLGs

The apparent density and swelling ratio of the CLGs are summarized in Table S2 (cf. ESM). The apparent density of the CLGs ranges from 0.0375 to 0.0686 g·cm⁻³, allowing it to be used as a support body for photothermal materials. The swelling ratio of the CLGs ranges from 20 to 33 g·g⁻¹, which is inversely connected with the amount of lignin, mainly ascribed to the elevation of the hydroxyl groups in the crosslinked system resulting in a denser crosslinked network. Furthermore, lignin is a hydrophobic backbone with plenty of the aromatic groups, the hydrophobicity of the hydrogel is enhanced with the addition of lignin, leading to a lower swelling ratio and smaller internal pore size, demonstrating that the saturated water content of the CLGs can be regulated by adjusting the lignin content. The high swelling ratio of the material guarantees that water can be effectively transported to the interface of the evaporator throughout the evaporation process, ensuring the continuing solar-driven vapor generation process.

3.6 Light absorption properties and thermal conductivity of the CLGs

Efficient light absorption in the full spectrum (300–2500 nm) of the photothermal materials is necessary. The

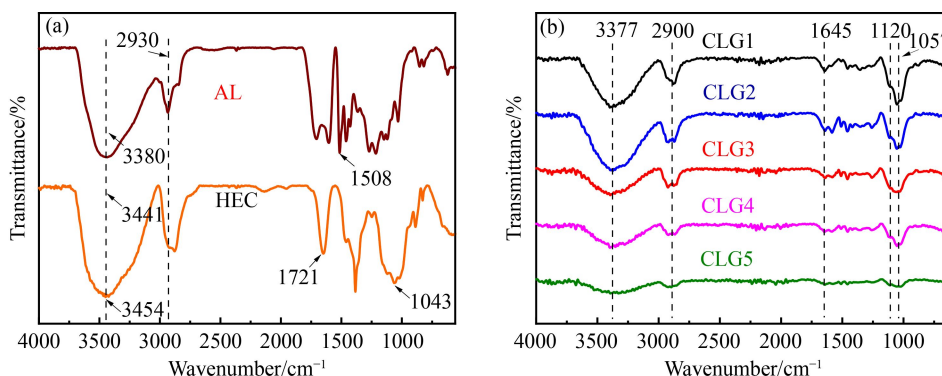


Fig. 4 FTIR spectra of the (a) HEC and AL and (b) CLGs.

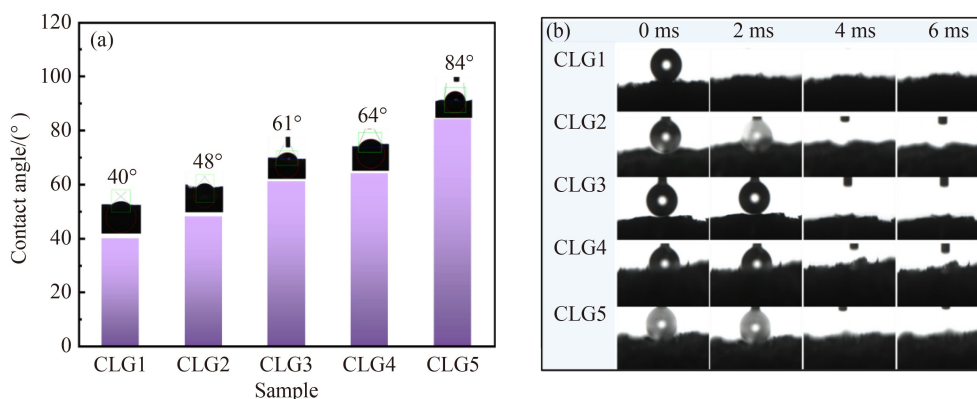


Fig. 5 (a) Surface water contact angle of CLGs; (b) internal wettability test of the CLGs.

ultraviolet–visible near infrared diffuse reflection and the thermal conductivity of the CLGs are shown in Fig. 6. Considering that GO with a two-dimensional structure can enhance the absorption of the solar energy through π - π^* electron leap. Hence, all hydrogel possesses a high light absorption rate of more than 97% in the wavelength range of 300–2500 nm (Fig. 6(a)). It is worth noting that the light absorption of CLG5 (98.2%) is higher than CLG1 (97.8%), indicating that the photothermal performance of the materials can be improved by the addition of lignin, demonstrating the synergistic effect of GO and AL in the photothermal conversion process [33]. The excellent light absorbance capacity of the CLGs offers a stable foundation for the subsequent photothermal evaporation process. The thermal conductivity of the photothermal materials can highly influence the photothermal evaporation process. An evaporator with low thermal conductivity can effectively reduce the heat transfer from the material to the water body so that more heat can be employed for the vapor generation. The CLGs exhibited low thermal conductivity (Fig. 6(b)) ranging from 0.04 to 0.05 $\text{W}\cdot\text{m}^{-1}\cdot\text{K}^{-1}$ and significantly lower than water (0.59 $\text{W}\cdot\text{m}^{-1}\cdot\text{K}^{-1}$), which indicates that the lignin content has no influence on the thermal conductivity of the materials. The results reveal that the synthesized photothermal material with outstanding thermal insulation properties can be applied as a competitive photothermal interfacial evaporator.

3.7 Equivalent evaporation enthalpy of the CLGs

Liquid water molecules are connected by hydrogen bonding during the evaporation process, forming clusters of the water molecules inside the hydrogel with minimal energy through conformational changes (Fig. 7). These clusters of the water molecules can evaporate more easily when they are constrained by the molecular lattice of the hydrogel, thus reducing the evaporation enthalpy of water (Fig. 7(a)) [44–46]. The dark field evaporation rates and equivalent evaporation enthalpy of the water and CLGs are shown in Fig. 7(b). The energy required for water

evaporation in the CLGs is less than that required for theoretical evaporation of water ($2436 \text{ J}\cdot\text{g}^{-1}$) at the same energy input, so the evaporation rate of water is boosted (Fig. 7(c)) [47]. The evaporation enthalpy of water in the CLGs gel network was measured by DSC (Fig. S2, cf. ESM) to clarify the role of crosslinked structures in CLGs for the evaporation process. Only a sharp peak is recorded during the evaporation of pure water, and the heat flow rate drops fast after the signal reaches its maximum, indicating that the water evaporation is completed immediately. However, the heat flow rate of the CLGs decays slowly, which is ascribed to the fact that three types of water (bound water, intermediate water and free water) are contained in the hydrogel structure, thus reducing the evaporation enthalpy of the water [48]. Results of evaporation enthalpy of DSC and dark field experiments are summarized in Table S3 (cf. ESM). The evaporation enthalpy calculated by DSC is higher than that obtained by the dark field evaporation because of the presence of dehydration during the test. Consequently, the results of dark field evaporation experiments are exceedingly accurate.

3.8 Photothermal evaporation performance of the CLGs

The above characterization demonstrates that CLGs own uniform internal channels, superior water transport capacity, excellent light absorption capacity and low thermal conductivity, which can provide effective photothermal evaporation foundation for desalination. Photothermal evaporation experiments of the CLGs under different conditions are illustrated in Fig. 8. The photothermal evaporation performance of the CLGs with varying lignin concentrations was measured under 1 sun irradiation (Fig. 8(a)). The evaporation rates of the CLG1, CLG2, CLG3, CLG4, and CLG5 are 1.83, 1.93, 2.33, 2.55, and 2.46 $\text{kg}\cdot\text{m}^{-2}\cdot\text{h}^{-1}$, respectively, indicating that the surface temperature of the CLGs rises rapidly under sunlight irradiation and possess excellent photothermal conversion capability. In addition, extraordinarily hydrophilic and rich pore structures can continually transport water to the

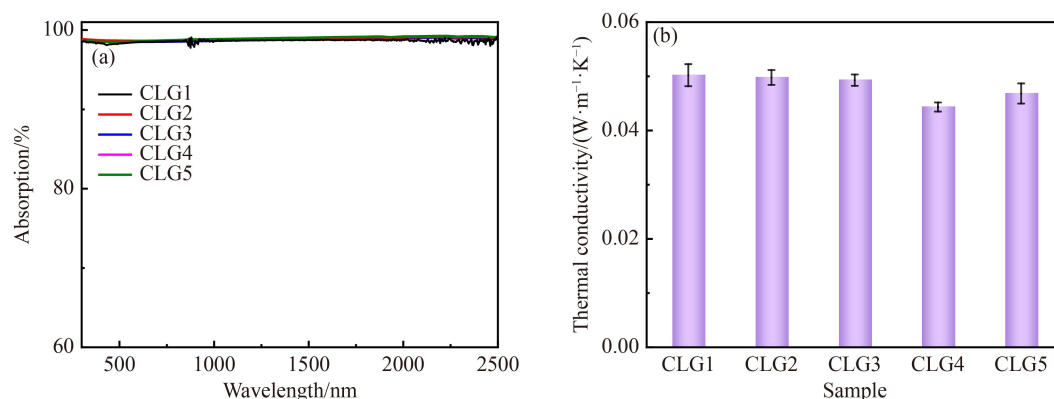


Fig. 6 (a) Light absorption spectra of the CLGs in the wavelength range of 300–2500 nm; (b) thermal conductivity of the CLGs.

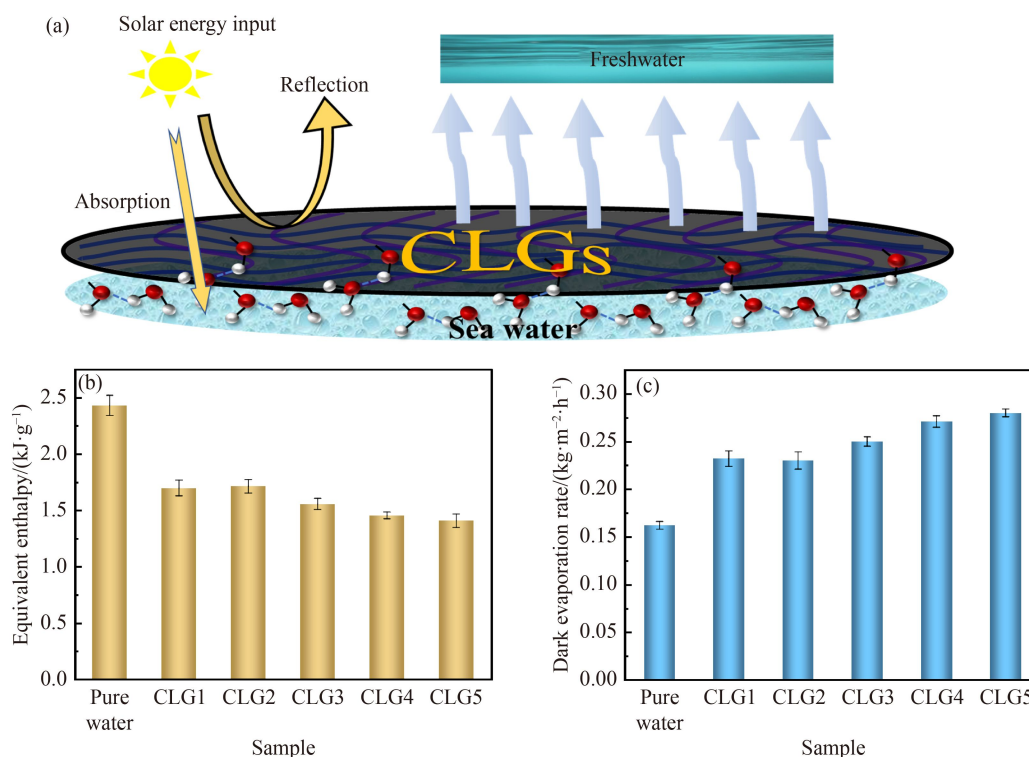


Fig. 7 (a) Illustration of photothermal evaporation process; (b) equivalent evaporation enthalpy of the water and CLGs; (c) water evaporation rate of the water and CLGs in dark condition.

interface of the evaporator and allow vapor to escape through these pores [49]. Temperature change profiles (Fig. 8(b)) and infrared images (Fig. 8(c)) of the CLGs were recorded using an infrared camera. The surface temperature of the CLG1, CLG2, CLG3, CLG4, and CLG5 rapidly warmed up to 33.0, 32.5, 33.4, 35.7 and 36.1 °C within 1 min. After 10 min, the temperature was elevated to 36.8, 38.2, 39.3, 40.3 and 43.8 °C, and reached equilibrium at 30 min. Due to the photothermal ability of the lignin, its higher content can improve the photothermal capacity of the hydrogel and rise the surface temperature of the evaporator. The solar evaporation rate and efficiency of the CLGs are shown in Fig. 9. The highest evaporation rate was found on the CLG4 ($2.55 \text{ kg}\cdot\text{m}^{-2}\cdot\text{h}^{-1}$), which is 4.4 times higher than water ($0.53 \text{ kg}\cdot\text{m}^{-2}\cdot\text{h}^{-1}$). The calculated result shows that the solar evaporation efficiency of CLG1–CLG5 is 75.1%, 81.2%, 89.7%, 92.1% and 84.9%, respectively (Fig. 9(a)). The increase in lignin content enhances the photothermal conversion performance of the CLGs, the thermal energy absorbed by the CLGs is more concentrated for photothermal evaporation, and the water evaporation rate is improved. Although the highest surface temperature (46.8 °C) of the CLG5 can be attained after 60 min, the water transport performance declined compared to the CLG4, and it might not timely and effectively carry out the evaporation process. The comparison of evaporation performance of CLG4 and previous work is summarized in Table 1, suggesting that the synthesized CLG4 is a

competitive photothermal evaporator. The interfacial evaporation performance of the CLG4 under various light-intensity situations was investigated (Fig. 9(b)). It is found that brighter light could bring quicker evaporation rates. The water evaporation rates of the CLG4 were 4.21 and $5.37 \text{ kg}\cdot\text{m}^{-2}\cdot\text{h}^{-1}$ under 2 and 3 suns, respectively. Cycling tests were conducted on the materials to establish the potential application capability of the CLG4 (Fig. 9(c)). Given the stable photothermal conversion ability of the GO within the hydrogels, as well as the excellent water transport performance of the CLG4, the water evaporation rate of the hydrogel is in the range of 2.45 – $2.59 \text{ kg}\cdot\text{m}^{-2}\cdot\text{h}^{-1}$ in five cycles, and the apparent shape of the material did not change significantly, which indicated the excellent stability of the evaporator. Artificial seawater was employed to investigate the potentially practical application of the CLG4 in the real desalination process, and the water vapor produced during the evaporation process is collected in a simple distillation device (Fig. S3, cf. ESM). The concentrations of cations (Na^+ , K^+ , Ca^{2+} and Mg^{2+}) before and after evaporation can be seen in Fig. 9(d) and Table S4 (cf. ESM). The removal ratio of the cations in the water is greatly increased to over 99% after evaporation, meeting the criterion of the human drinking water [50].

3.9 Salt resistance performance of CLG4

The solar evaporation performance of the CLG4 in

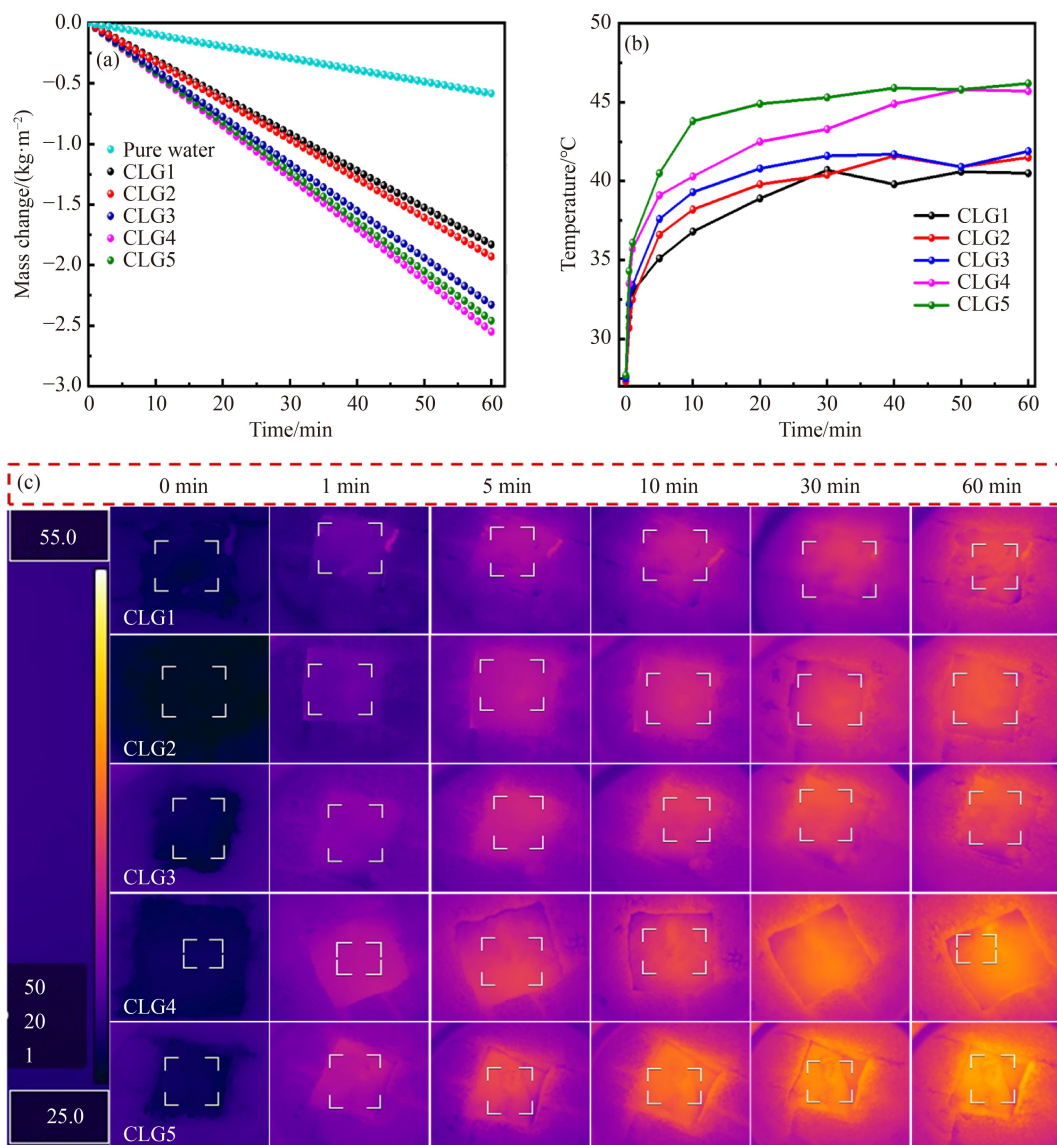


Fig. 8 (a) The mass change of water under 1 sun; (b) the surface temperature rises of the CLGs relative to heating time under 1 sun; (c) the infrared photographs of the CLGs surface in different times under 1 sun.

different concentrations of NaCl solution (3.5, 7.0, 10, and 20 wt %) was tested to explore the potential practical application capacity in high salt concentration water, which is illustrated in Fig. S4 (cf. ESM). The solar evaporation rate of the CLG4 is $2.44 \text{ kg}\cdot\text{m}^{-2}\cdot\text{h}^{-1}$ under 1 sun in 3.5 wt % NaCl solution, which was slightly lower than that in water ($2.55 \text{ kg}\cdot\text{m}^{-2}\cdot\text{h}^{-1}$), indicating the superior evaporation performance of CLG4 applications in the evaporation process of seawater. The evaporation rates of the CLG4 in 7.0, 10, and 20 wt % salt solutions are 2.16, 2.02, and $1.89 \text{ kg}\cdot\text{m}^{-2}\cdot\text{h}^{-1}$, respectively. The good salt-resistance of the evaporator can be ascribed to the reason that the hydrophilic outer surface of the CLG4 provides for faster dissolution and transport of salts into the seawater bulk during evaporation process. Although increasing concentration of the NaCl solution decreases the solar evaporation rate of the material, the designed

material is suitable for the natural seawater desalination process.

4 Conclusions

Overall, lignin-based hydrogels with superior evaporation performance were successfully prepared by a simple sol-gel process for water purification. The solar evaporation efficiency and water evaporation rate of the CLG4 with the greatest capability can reach 92.1% and $2.55 \text{ kg}\cdot\text{m}^{-2}\cdot\text{h}^{-1}$ respectively under 1 sun. The effect of the lignin on the physicochemical properties and photothermal performance of the hydrogels was evaluated, demonstrating that the addition of lignin enhanced the mechanical properties, reduced the surface hydrophilicity and improved the water transport capacity

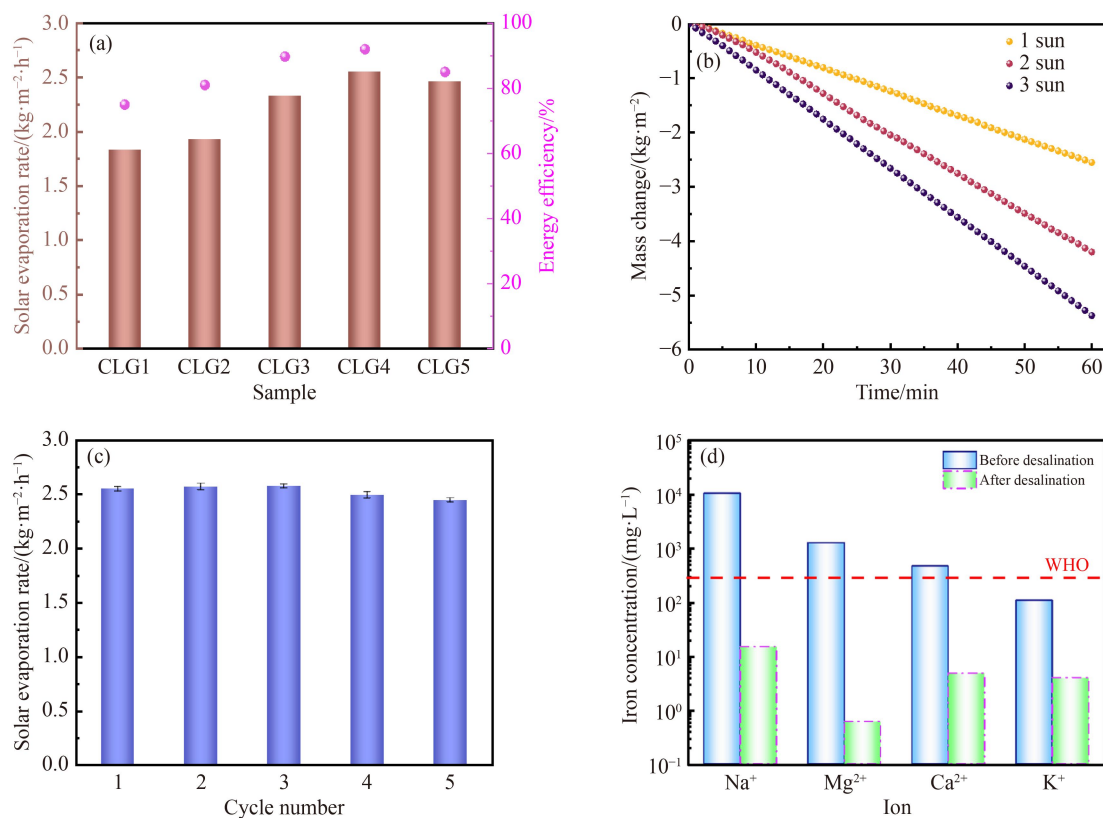


Fig. 9 (a) The evaporation rate and efficiency of the CLGs under 1 sun; (b) the evaporation rate of the CLG4 under different sunlight intensity; (c) the circulating water evaporation data of the CLG4; (d) concentrations of ions in the artificial seawater via solar evaporation using the CLG4.

Table 1 The comparison of evaporation performance of CLG4 under 1 sun and previous work

Samples	Evaporation rate/(kg·m ⁻² ·h ⁻¹)	Evaporation efficiency/%	Ref.
Lignin hydrogel-based evaporator	2.25	91.6	[32]
Biomass-derived evaporator	1.78	90.6	[51]
MnO ₂ NWs/chitosan hydrogels	1.72	92.5	[52]
Biomass photothermal evaporator	1.42	89.3	[53]
Hydrogel-derived evaporator	1.35	83	[54]
CLG4	2.55	92.1	This work

of the hydrogels. The high thermal insulation, rapid water transportation, and the synergistic effect of GO and AL in the photothermal process all contribute to the superior evaporation performance of the hydrogels. The concentration of cations in artificial seawater is greatly reduced with the removal ratio more than 99% after water purification and the solar evaporation rate of the hydrogel can maintain in the range of 2.45–2.59 kg·m⁻²·h⁻¹ in five cycles, suggesting the superior desalination performance and sustainability of the CLG4. This low-cost biomass-based hydrogel provides a new pathway for synthesizing efficient solar evaporator and a sustainable strategy for water purification.

Conflicts of interest There are no conflicts to declare.

Acknowledgements This work was supported by the Natural Science

Foundation of Guangdong, China (Grant No. 2022A1515010757), the National Key Research and Development Plan (Grant No. 2018YFB1501503) and the Science and Technology Program of Guangdong, China (Grant No. 2020B1111380002).

Electronic Supplementary Material Supplementary material is available in the online version of this article at <https://doi.org/10.1007/s11705-023-2311-2> and is accessible for authorized users.

References

1. Salehi M. Global water shortage and potable water safety: today's concern and tomorrow's crisis. *Environment International*, 2022, 158: 106936
2. Wang G, Yan T, Shen J, Zhang J, Shi L, Zhang D. Beneficial synergy of adsorption-intercalation-conversion mechanisms in Nb₂O₅@nitrogen-doped carbon frameworks for promoted

- removal of metal ions via hybrid capacitive deionization. *Environmental Science: Nano*, 2021, 8(1): 122–130
- Bartram J, Brocklehurst C, Fisher M B, Luyendijk R, Hossain R, Wardlaw T, Gordon B. Global monitoring of water supply and sanitation: history, methods and future challenges. *International Journal of Environmental Research and Public Health*, 2014, 11(8): 8137–8165
 - Huang L, Yan T, Mahmoud A E D, Li S, Zhang J, Shi L, Zhang D. Enhanced water purification via redox interfaces created by an atomic layer deposition strategy. *Environmental Science: Nano*, 2021, 8(4): 950–959
 - Kim K, Yu S, An C, Kim S W, Jang J H. Mesoporous three-dimensional graphene networks for highly efficient solar desalination under 1 sun illumination. *ACS Applied Materials & Interfaces*, 2018, 10(18): 15602–15608
 - Bai H, He P, Hao L, Fan Z, Niu R, Tang T, Gong J. Waste-treating-waste: upcycling discarded polyester into metal-organic framework nanorod for synergistic interfacial solar evaporation and sulfate-based advanced oxidation process. *Chemical Engineering Journal*, 2023, 456: 140994
 - Anis S F, Hashaikeh R, Hilal N. Functional materials in desalination: a review. *Desalination*, 2019, 468: 114077
 - Panchal H N, Patel S. An extensive review on different design and climatic parameters to increase distillate output of solar still. *Renewable & Sustainable Energy Reviews*, 2017, 69: 750–758
 - Chen L, Ren J, Gong J, Qu J, Niu R. Cost-effective, scalable fabrication of self-floating xerogel foam for simultaneous photothermal water evaporation and thermoelectric power generation. *Chemical Engineering Journal*, 2023, 454: 140383
 - Garg K, Khullar V, Das S K, Tyagi H. Performance evaluation of a brine-recirculation multistage flash desalination system coupled with nanofluid-based direct absorption solar collector. *Renewable Energy*, 2018, 122: 140–151
 - Chowdhury M R, Steffes J, Huey B D, McCutcheon J R. 3D printed polyamide membranes for desalination. *Science*, 2018, 361(6403): 682–686
 - Zhang P, Liao Q, Yao H, Huang Y, Cheng H, Qu L. Direct solar steam generation system for clean water production. *Energy Storage Materials*, 2019, 18: 429–446
 - Chen C, Kuang Y, Hu L. Challenges and opportunities for solar evaporation. *Joule*, 2019, 3(3): 683–718
 - Fan Z, Ren J, Bai H, He P, Hao L, Liu N, Chen B, Niu R, Gong J. Shape-controlled fabrication of MnO/C hybrid nanoparticle from waste polyester for solar evaporation and thermoelectricity generation. *Chemical Engineering Journal*, 2023, 451: 138534
 - Blanco-Marigorta A M, Lozano-Medina A, Marcos J D. A critical review of definitions for exergetic efficiency in reverse osmosis desalination plants. *Energy*, 2017, 137: 752–760
 - Choi S H. On the brine re-utilization of a multi-stage flashing (MSF) desalination plant. *Desalination*, 2016, 398: 64–76
 - Wang F, Cheng Z, Tan J, Yuan Y, Yong S, Liu L. Progress in concentrated solar power technology with parabolic trough collector system: a comprehensive review. *Renewable & Sustainable Energy Reviews*, 2017, 79: 1314–1328
 - Kunwer R, Pandey S, Pandey G. Technical challenges and their solutions for integration of sensible thermal energy storage with concentrated solar power applications—a review. *Process Integration and Optimization for Sustainability*, 2022, 6(3): 559–585
 - Kiriarachchi H D, Hassan A A, Awad F S, El-Shall M S. Metal-free functionalized carbonized cotton for efficient solar steam generation and wastewater treatment. *RSC Advances*, 2021, 12(2): 1043–1050
 - Zhu L, Gao M, Peh C K N, Ho G W. Solar-driven photothermal nanostructured materials designs and prerequisites for evaporation and catalysis applications. *Materials Horizons*, 2018, 5(3): 323–343
 - Fan H, Gao A, Zhang G, Zhao S, Cui J, Yan Y. A design of bifunctional photothermal layer on polysulfone membrane with enclosed cellular-like structure for efficient solar steam generation. *Chemical Engineering Journal*, 2021, 415: 128798
 - Xiao C, Chen L, Mu P, Jia J, Sun H, Zhu Z, Liang W, Li A. Sugarcane-based photothermal materials for efficient solar steam generation. *ChemistrySelect*, 2019, 4(27): 7891–7895
 - Liu Y, Yu S, Feng R, Bernard A, Liu Y, Zhang Y, Duan H, Shang W, Tao P, Song C, Deng T. A bioinspired, reusable, paper-based system for high-performance large-scale evaporation. *Advanced Materials*, 2015, 27(17): 2768–2774
 - Joo B S, Kim I S, Ki Han I, Ko H, Gu Kang J, Kang G. Plasmonic silicon nanowires for enhanced heat localization and interfacial solar steam generation. *Applied Surface Science*, 2022, 583: 152563
 - Huang W, Su P, Cao Y, Li C, Chen D, Tian X, Su Y, Qiao B, Tu J, Wang X. Three-dimensional hierarchical Cu_xS-based evaporator for high-efficiency multifunctional solar distillation. *Nano Energy*, 2020, 69: 104465
 - Zhang P, Xie M, Jin Y, Jin C, Wang Z. A bamboo-based photothermal conversion device for efficient solar steam generation. *ACS Applied Polymer Materials*, 2022, 4(4): 2393–2400
 - Zhong D, Liu Q, Zheng D. Synthesis of lignin-grafted polycarboxylate superplasticizer and the dispersion performance in the cement paste. *Colloids and Surfaces A*, 2022, 642: 128689
 - Yu M, Mishra D, Cui Z, Wang X, Lu Q. Recycling papermill waste lignin into recyclable and flowerlike composites for effective oil/water separation. *Composites Part B: Engineering*, 2021, 216: 108884
 - Chen J, An L, Heo J W, Bae J H, Jeong H, Kim Y S. Utilization of aminated lignin as an adsorbent to remove cationic and anionic dyes from aqueous solutions. *Journal of Wood Chemistry and Technology*, 2022, 42(2): 114–124
 - Sun L, Mo Z, Li Q, Zheng D, Qiu X, Pan X. Facile synthesis and performance of pH/temperature dual-response hydrogel containing lignin-based carbon dots. *International Journal of Biological Macromolecules*, 2021, 175: 516–525
 - Li Y, Yang D, Li P, Li Z. Lignin as a multi-functional agent for the synthesis of Ag nanoparticles and its application in antibacterial coatings. *Journal of Materials Research and Technology*, 2022, 17: 3211–3220
 - Jiang S, Zhang Z, Zhou T, Duan S, Yang Z, Ju Y, Jia C, Lu X, Chen F. Lignin hydrogel-based solar-driven evaporator for cost-effective and highly efficient water purification. *Desalination*,

- 2022, 531: 115706
33. Zhao X, Huang C, Xiao D, Wang P, Luo X, Liu W, Liu S, Li J, Li S, Chen Z. Melanin-inspired design: preparing sustainable photothermal materials from lignin for energy generation. *ACS Applied Materials & Interfaces*, 2021, 13(6): 7600–7607
 34. Huang S, Wu L, Li T, Xu D, Lin X, Wu C. Facile preparation of biomass lignin-based hydroxyethyl cellulose super-absorbent hydrogel for dye pollutant removal. *International Journal of Biological Macromolecules*, 2019, 137: 939–947
 35. Wu L, Huang S, Zheng J, Qiu Z, Lin X, Qin Y. Synthesis and characterization of biomass lignin-based PVA super-absorbent hydrogel. *International Journal of Biological Macromolecules*, 2019, 140: 538–545
 36. Bidgoli H, Mortazavi Y, Khodadadi A A. A functionalized nanostructured cellulosic sorbent aerogel for oil spill cleanup: synthesis and characterization. *Journal of Hazardous Materials*, 2019, 366: 229–239
 37. Wang C, Xiong Y, Fan B, Yao Q, Wang H, Jin C, Sun Q. Cellulose as an adhesion agent for the synthesis of lignin aerogel with strong mechanical performance, sound-absorption and thermal insulation. *Scientific Reports*, 2016, 6(1): 32383
 38. Xie Z, Zhu J, Zhang L. Three-dimensionally structured polypyrrole-coated setaria viridis spike composites for efficient solar steam generation. *ACS Applied Materials & Interfaces*, 2021, 13(7): 9027–9035
 39. Tang J, Javaid M U, Pan C, Yu G, Berry R M, Tam K C. Self-healing stimuli-responsive cellulose nanocrystal hydrogels. *Carbohydrate Polymers*, 2020, 229: 115486
 40. Ravishankar K, Venkatesan M, Desingh R P, Mahalingam A, Sadhasivam B, Subramaniam R, Dhamodharan R. Biocompatible hydrogels of chitosan-alkali lignin for potential wound healing applications. *Materials Science and Engineering C*, 2019, 102: 447–457
 41. Dai L, Zhu W, Lu J, Kong F, Si C, Ni Y. A lignin-containing cellulose hydrogel for lignin fractionation. *Green Chemistry*, 2019, 21(19): 5222–5230
 42. Rong K, Wei J, Wang Y, Liu J, Qiao Z A, Fang Y, Dong S. Deep eutectic solvent assisted zero-waste electrospinning of lignin fiber aerogels. *Green Chemistry*, 2021, 23(16): 6065–6075
 43. Feng C, Ren P, Li Z, Tan W, Zhang H, Jin Y, Ren F. Graphene/waste-newspaper cellulose composite aerogels with selective adsorption of organic dyes: preparation, characterization, and adsorption mechanism. *New Journal of Chemistry*, 2020, 44(6): 2256–2267
 44. Zhao F, Zhou X, Shi Y, Qian X, Alexander M, Zhao X, Mendez S, Yang R, Qu L, Yu G. Highly efficient solar vapour generation via hierarchically nanostructured gels. *Nature Nanotechnology*, 2018, 13(6): 489–495
 45. Zhou X, Zhao F, Guo Y, Zhang Y, Yu G. A hydrogel-based antifouling solar evaporator for highly efficient water desalination. *Energy & Environmental Science*, 2018, 11(8): 1985–1992
 46. Zhou X, Guo Y, Zhao F, Yu G. Hydrogels as an emerging material platform for solar water purification. *Accounts of Chemical Research*, 2019, 52(11): 3244–3253
 47. Yao H, Zhang P, Yang C, Liao Q, Hao X, Huang Y, Zhang M, Wang X, Lin T, Cheng H, Yuan J, Qu L. Janus-interface engineering boosting solar steam towards high-efficiency water collection. *Energy & Environmental Science*, 2021, 14(10): 5330–5338
 48. Guo Y, Zhou X, Zhao F, Bae J, Rosenberger B, Yu G. Synergistic energy nanoconfinement and water activation in hydrogels for efficient solar water desalination. *ACS Nano*, 2019, 13(7): 7913–7919
 49. Lu Y, Wang X, Fan D, Yang H, Xu H, Min H, Yang X. Biomass derived janus solar evaporator for synergic water evaporation and purification. *Sustainable Materials and Technologies*, 2020, 25: e00180
 50. Jiang F, Liu H, Li Y, Kuang Y, Xu X, Chen C, Huang H, Jia C, Zhao X, Hitz E, Zhou Y, Yang R, Cui L, Hu L. Lightweight, mesoporous, and highly absorptive all-nanofiber aerogel for efficient solar steam generation. *ACS Applied Materials & Interfaces*, 2018, 10(1): 1104–1112
 51. Fang Q, Li T, Chen Z, Lin H, Wang P, Liu F. Full biomass-derived solar stills for robust and stable evaporation to collect clean water from various water-bearing media. *ACS Applied Materials & Interfaces*, 2019, 11(11): 10672–10679
 52. Irshad M S, Wang X, Abbasi M S, Arshad N, Chen Z, Guo Z, Yu L, Qian J, You J, Mei T. Semiconductive, flexible MnO₂ NWs/chitosan hydrogels for efficient solar steam generation. *ACS Sustainable Chemistry & Engineering*, 2021, 9(10): 3887–3900
 53. Li J, Zhou X, Zhang J, Liu C, Wang F, Zhao Y, Sun H, Zhu Z, Liang W, Li A. Migration crystallization device based on biomass photothermal materials for efficient salt-ejection solar steam generation. *ACS Applied Energy Materials*, 2020, 3(3): 3024–3032
 54. Guo Y, Bae J, Fang Z, Li P, Zhao F, Yu G. Hydrogels and hydrogel-derived materials for energy and water sustainability. *Chemical Reviews*, 2020, 120(15): 7642–7707